

Vortex Dynamics from Burst-and-Coast Motion of Anguilliform and Carangiform Swimmers

Zahra Maleksabet¹, Maham Kamran¹, Ali Tarokh², and Muhammad Saif Ullah Khalid^{1*}

¹Nature-Inspired Engineering Research Lab (NIERL), Department of Mechanical and Mechatronics Engineering, Lakehead University, Thunder Bay, ON P7B 5E1, Canada

²Department of Mechanical and Mechatronics Engineering, Lakehead University, Thunder Bay, ON P7B 5E1, Canada

*Corresponding Author, Email: mkhalid7@lakeheadu.ca

Abstract

Fish perform various propulsive maneuvers while swimming by generating traveling waves along their bodies and producing thrust through tail strokes. Anguilliform swimmers spread motion along the body, while carangiform swimmers' motion is more prominent near their tails. Many species also switch between continuous undulation and intermittent swimming, such as burst-and-coast maneuver, which can save energy but can also change the wake structure and hydrodynamic forces. Our current study aims at explaining how duty cycle (DC), undulatory gaits, and Strouhal number (St), shape the near-body vortices, overall wakes, and the hydrodynamic forces. We carry out three-dimensional simulations at $Re = 3000$ for flows around an eel (anguilliform) and a Jack Fish (carangiform) for $DC = 0.2 - 1.0$ and $St = 0.30$ and 0.40 . Our results reveal that the burst-and-coast motion for both swimmer produce bow-shaped wakes, the two rows of which on the sides approach each other to form a more coherent wake as DC is increased to 1.0 that corresponds to the wake of continuously undulating swimmers. It is also found that the intermittent motion at a higher Strouhal number produces more drag, contrary to the continuous undulatory kinematics. We further investigate this behavior by quantifying the strengths of vortices produced around the two swimmers and their instantaneous kinematic metrics. A detailed analysis for the role of different body sections in the production of unsteady streamwise forces is also presented. These insights provide important connections between the swimmers' physiologies, their kinematics, and the governing vortex dynamics to attain certain hydrodynamic metrics for designing next-generation autonomous bio-inspired underwater robots.

1 Introduction

For the past several decades, aquatic locomotion is a subject of intensive scientific investigations, because it couples biology and fluid dynamics for a single, richly unsteady phenomenon. Fish achieve efficient propulsion through body–flow interactions that redistribute momentum via coherent vortices formed along the body and shed from the caudal fin in the wake. The principles and lessons learnt from hydrodynamics of fish, inform the design of bio-inspired underwater vehicles and autonomous robots that must balance endurance, maneuverability, and controllability in complex environments. Intermittent gaits are especially attractive from an energy-management perspective, and a deeper understanding of how near-body vortices organize thrust, drag, and side forces can translate directly into actuation strategies for fast and efficient propulsion in engineered systems.

Among undulatory strategies, anguilliform and carangiform swimming modes represent two canonical gait families distinguished by both morphology and kinematics. Anguilliform swimmers like eels undergo large-amplitude undulations distributed almost uniformly along the full body-length, generating thrust and creating intricate, spatially and temporally evolving flow features along the body and in the wakes [1]. Simulations and experiments showed that this distributed actuation promoted the formation, convection, and interaction of body-attached vortices to modulate pressure over extended surface regions, yielding unsteady but sustained propulsive output [2, 3]. Contrarily, carangiform swimmers

like Jack fish concentrate most of the undulatory motion in the posterior part of the body. The anterior body remains comparatively rigid, while the peduncle and caudal fin execute large-amplitude oscillations [3, 4]. These differences in profile of the undulation amplitude, effective wavelength, and kinematics of the caudal fin strongly influence power consumption and attainable swimming speeds. Particularly, intermittent burst-and-coast locomotion is widely observed in both gait families and plays a central role in energy management [5]. During the burst phase, active undulations produce large circulation and high instantaneous thrust. During the coast phase, the body becomes effectively rigid and straight, and it moves within the previously generated momentum field. Some previous studies suggested that alternating between these phases reduced average muscular effort and overall metabolic cost relative to strictly continuous undulation [5–7], with some energy saved due to the inertial wake generated in the burst phase [8, 9]. Continuous gaits tend to produce regular shedding coherent flow structures, whereas burst-and-coast strategies introduce transient amplification of vortex structures as the body is alternately driven in the two phases. These differences are expressed directly in temporal profiles of thrust, drag, and side-force.

Most of the previous investigations focused on examining the vortex dynamics and its influence on the hydrodynamic performance of fish, performing continuous undulations [3, 10–13]. Besides, there exist a few studies that explored the fluid dynamics and quantifying the associated benefits of intermittent swimming of two-dimensional undulating bodies in terms of energy expenditures [5, 7–9, 14]. These studies suffer from limitations, such as the utilization of inviscid flow based modeling techniques, and simple two-dimensional foil-like geometric bodies, which do not capture the complex vortex-body and vortex-vortex interactions, happening around real marine organisms. According to the authors’ knowledge, there exists no study in the current literature that explains the three-dimensional vortex dynamics and its role on production of instantaneous hydrodynamic forces of biological swimmers. Ashraf et al. [15] performed experiments and three-dimensional simulations for flows around a rummy nose tetra fish (*Hemigrammus bleheri*) to only examine the power requirements for various swimming modes, including burst-and-coast motion. With more interest arising in the marine engineering community to develop bio-inspired underwater robots, it is an important knowledge gap that our present study addresses here for two important classes of biological swimmers, including carangiform and anguilliform. The hierarchical relation between the duty cycle (defined as the fraction of the cycle spent in active undulation) and energy consumption by undulating swimmers was previously explained by Dai et al. [7] for two-dimensional elastic bodies and Liu et al. [5] for an experimental fish-inspired robot. Nevertheless, the combined effects of duty cycle and undulatory kinematic modes of swimmers along with their morphologies for different Strouhal numbers on hydrodynamics and forces are not elucidated earlier.

To investigate these important hydrodynamic aspects for biological swimmers and their bio-inspired counterpart robotic systems, we perform high-fidelity three-dimensional simulations around two different marine swimmers, including a Jack fish (*Crevalle Jack* or *Caranx Hippas*) and an American eel (*Anguilla Rostrata*), which are representatives of carangiform and anguilliform classes [3, 12], respectively. The primary aim of our present work is to examine the unsteady flow dynamics around the two physiologically and kinematically very different swimmers, while they perform the burst-and-coast motion as well as continuous undulations under varying Strouhal number. Our computational simulations using the in-house fully parallelized sharp-interface immersed-boundary solver, Vortexdyn, reveal intriguing similarities in the hydrodynamics of the two swimmers. Our further analyses also unveils key systematic variations in the wake dynamics of these swimmers with a consistent changes in duty cycle through their respective undulatory kinematic profiles.

2 Computational Methodology

In this study, we simulate three-dimensional flow around real geometries of two fish species, including the American eel and the Jack Fish, for which the morphological data for these swimmers is adopted

from the work previously done by Khalid et al. [3, 12]. The Jack Fish, consisting of trunk and caudal fin sections, has a total height and width of $0.3021L$ and $0.1481L$, respectively, with a body area of $0.4479L^2$. Here, L presents the body-length of a swimmer. Its surface mesh comprises 22,712 triangular elements for the trunk and 2,560 for the caudal fin. The eel has a slender geometry, with a total height and width of $0.0884L$ and $0.0605L$, respectively, with the surface area of $0.1739L^2$, which is discretized using 33,112 triangular elements.

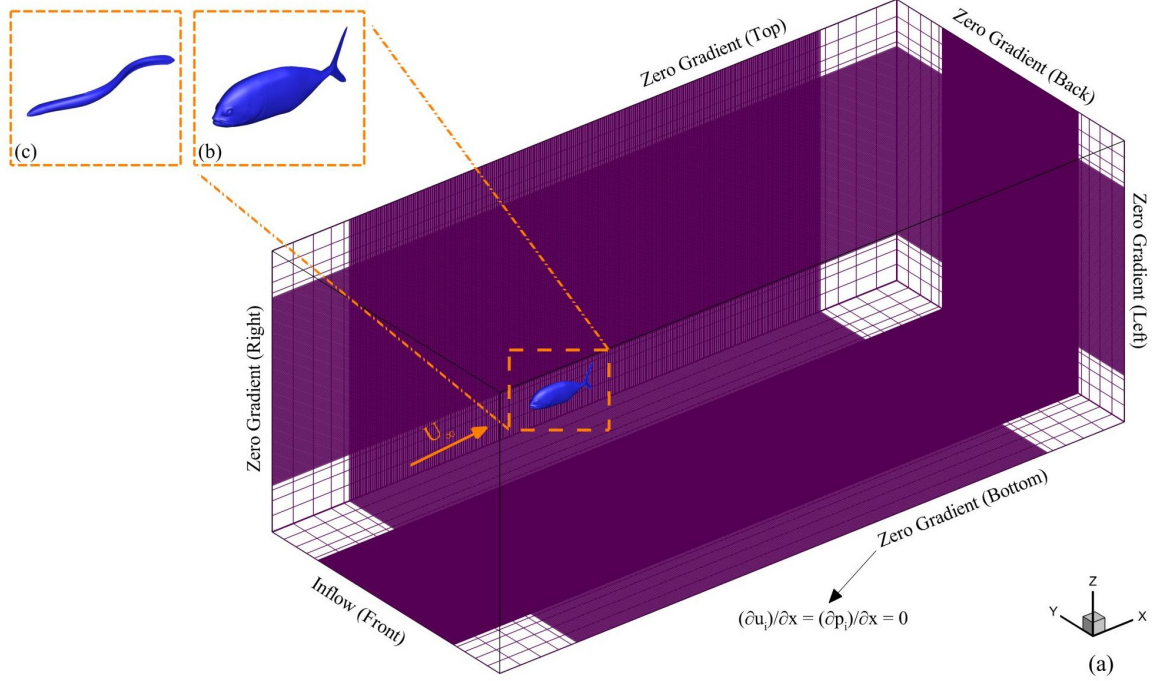


Figure 1: (a) Flow domain with specific boundary conditions on its sides and the mesh regions around a swimmer's body, (b) physiology of a Jack Fish, and (c) geometrical features of an eel

Each swimmer's body kinematics follow a wavy motion defined by a traveling wave function combined with a temporal smoothing function to transition between the burst and coast phases. This formulation is based on the approach proposed by Yang et al. [9]. Equation 1 describes the instantaneous local undulatory kinematics on each point on a swimmer's body.

$$y(x, t) = \begin{cases} S(t)A_m(x) \sin \left[2\pi \left(\frac{x}{\lambda} - \frac{t}{T_s} \right) - \frac{2\pi}{\lambda} \right], & 0 \leq t \leq T_s, \\ 0, & T_s < t \leq T, \end{cases} \quad (1)$$

where the oscillation amplitude A_m as a function of the location of a point on the body is provided below using second-order polynomials for the carangiform motion [3, 16]:

$$A \left(\frac{x}{L} \right) = 0.02 - 0.0825 \left(\frac{x}{L} \right) + 0.1625 \left(\frac{x}{L} \right)^2; \quad 0 < \frac{x}{L} < 1 \quad (2)$$

For the anguilliform motion, A_m is defined as [12]:

$$A \left(\frac{x}{L} \right) = 0.0367 + 0.0323 \left(\frac{x}{L} \right) + 0.0310 \left(\frac{x}{L} \right)^2; \quad 0 < \frac{x}{L} < 1 \quad (3)$$

A cosine-based smoothing function in Eq. 4 modulates the undulatory kinematics during the burst phase:

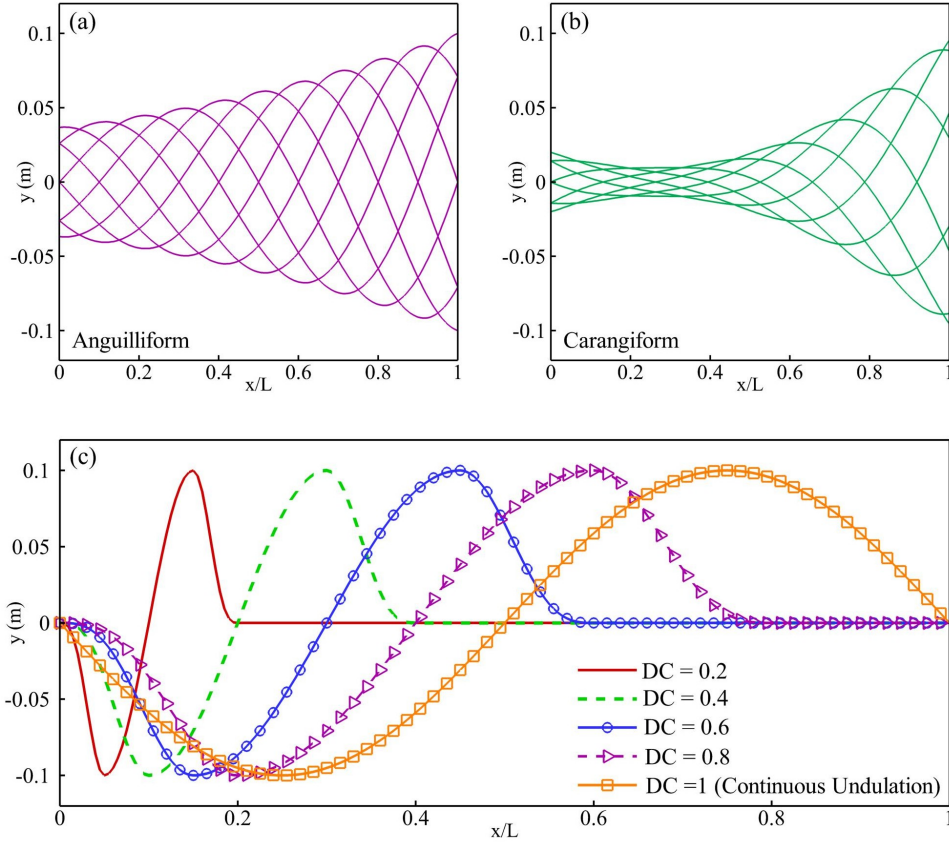


Figure 2: Undulatory kinematic profiles for the (a) anguilliform and (b) carangiform modes, and (c) the kinematic profiles of the swimmer's tail during burst-and-coast motion with different duty cycles

$$S(t) = \begin{cases} 0.5 \left[1 - \cos\left(\frac{4\pi t}{T_s}\right) \right], & 0 \leq t \leq 0.25T_s, \\ 1, & 0.25T_s < t \leq 0.75T_s, \\ 0.5 \left[1 - \cos\left(\frac{4\pi t}{T_s}\right) \right], & 0.75T_s < t \leq T_s. \end{cases} \quad (4)$$

In the equations above, t is the time, λ denotes the wavelength of the traveling wave along a swimmer's body, T_s shows the time for the burst phase in one full burst-and-coast cycle, for which T is the total period. Therefore, the non-dimensional quantity, duty cycle (DC), represents the fraction of the time spent for active undulation within a swimming cycle [14]. It is defined below:

$$DC = \frac{\text{Time for active undulation during burst}}{\text{total time for one burst-and-coast cycle}} = \frac{T_s}{T} \quad (5)$$

The governing mathematical model for fluid flows is based on the following non-dimensional forms of the continuity and incompressible Navier-Stokes equations [17, 18]:

$$\begin{aligned} \frac{\partial u_j}{\partial x_j} &= 0, \\ \frac{\partial u_i}{\partial t} + u_j \frac{\partial u_i}{\partial x_j} &= -\frac{1}{\rho} \frac{\partial p}{\partial x_i} + \frac{1}{Re} \frac{\partial^2 u_i}{\partial x_j \partial x_j} + f_b \end{aligned} \quad (6)$$

where $i, j = 1, 2, 3$, x_i represents the Cartesian directions, u_i denotes the Cartesian components of velocity of the fluid, p is the pressure, and Re is the Reynolds number. We define it as $Re = U_\infty L / \nu$,

where U_∞ shows the free-stream velocity, and ν is kinematic viscosity of the fluid. In this formulation, f_b is a discrete forcing term that enables a sharp representation of the immersed boundary [17, 18].

We solve these equations using our in-house sharp-interface immersed boundary method (IBM) based solver, **VorteXdyn**, to accurately capture the interaction between the fluid and the complex geometry of the swimmers, containing volumetric parts and membranous elements [13, 17]. Spatial derivatives are discretized using the second-order central difference and Quadratic Upstream Interpolation for Convective Kinematics (QUICK) schemes for the diffusion and convective terms, respectively. Time marching in this solver is carried out using the fractional-step method that ensures second-order accuracy. Boundary conditions are imposed such that a Dirichlet condition is used for the inflow, while Neumann conditions are enforced at all other boundaries of the domain, as also explained in Fig. 1. No-slip boundary conditions are applied on the swimmer’s body using the ghost cell-based approach [17]. Further details on the verification and validation of the solver can be found in the studies by Farooq et al. [17] and Kamran et al. [19] to ensure the accuracy and reliability of our solver.

3 Results and Discussion

The primary objective of this work is to examine the three-dimensional vortex dynamics around swimmers and in their wakes and to focus on how hydrodynamic forces are influenced by these flow mechanisms while they perform burst-and-coast motion with different duty cycles. The governing flow and kinematic parameters used here are summarized in Table 1. The simulations here are conducted at $Re = 3,000$, lying within a transitional flow regime [10]. Previously, Liu et al. [11] and Zhong et al. [20] concluded that primary flow features around oscillating bodies remained the same with varying Reynolds number. Both carangiform and anguilliform waveforms are prescribed over the respective swimmers for Strouhal numbers (St) of 0.30 and 0.40, consistent with the typical swimming patterns of marine animals [11, 21]. Here, Strouhal number is defined as $St = 2A_o f / U_\infty$, where f presents the undulation frequency, and A_o is the maximum one-sided oscillation amplitude of the swimmer’s tail. It is important to note that the undulation wavelength is set to $\lambda / L = 0.80$ for the anguilliform kinematic mode [12] and $\lambda / L = 1.05$ for the carangiform mode [3, 11].

Table 1: Specifications of the governing parameters

Parameters	Specifications
Swimmers	Eel and Jack Fish
Undulatory kinematics	Anguilliform and Carangiform
Motion	Burst and Coast ($DC = 0.2 - 0.8$) & Continuous ($DC = 1$)
Re	3000
St	0.30 and 0.40
λ / L	0.80 (anguilliform) and 1.05 (carangiform)

We start the discussion by explaining the development of three-dimensional coherent flow features around the two swimmers for different undulatory kinematic profiles. Figure 3 provides visualizations of vortices around the anguilliform swimmer at the end of the undulation cycle in each case of DC and Strouhal number considered in this work. We notice that the swimmer forms bow-like wakes for $DC = 0.2 - 0.8$ (see Figs. 3a₁ to 3d₁ for $St = 0.30$ and Figs. 3a₂ to 3d₂ for $St = 0.40$). These wakes are constituted by two well-separated rows of vortices on either side of the body, angled outward with the row on the right that consistently gets formed at a slightly higher angle from the body. This asymmetry arises from the phase of the body’s oscillation and can get inverted laterally by introducing a phase of π in the undulatory profile. Close to the body, shear layers roll up into hairpin-like vortices, which get detached from the body and combine with trailing-edge vortices to form ring-like structures in the

wake. On the anterior side of the swimmer, there is always a shear layer due to the interaction between the flow and the body. As the duty cycle increases, these dual vortex rows shift closer to the swimmer's centerline (or that of the wake) while fewer vortices are shed per cycle, though the asymmetry in angles remains. Also, the vortex shedding process lasts less by increasing DC.

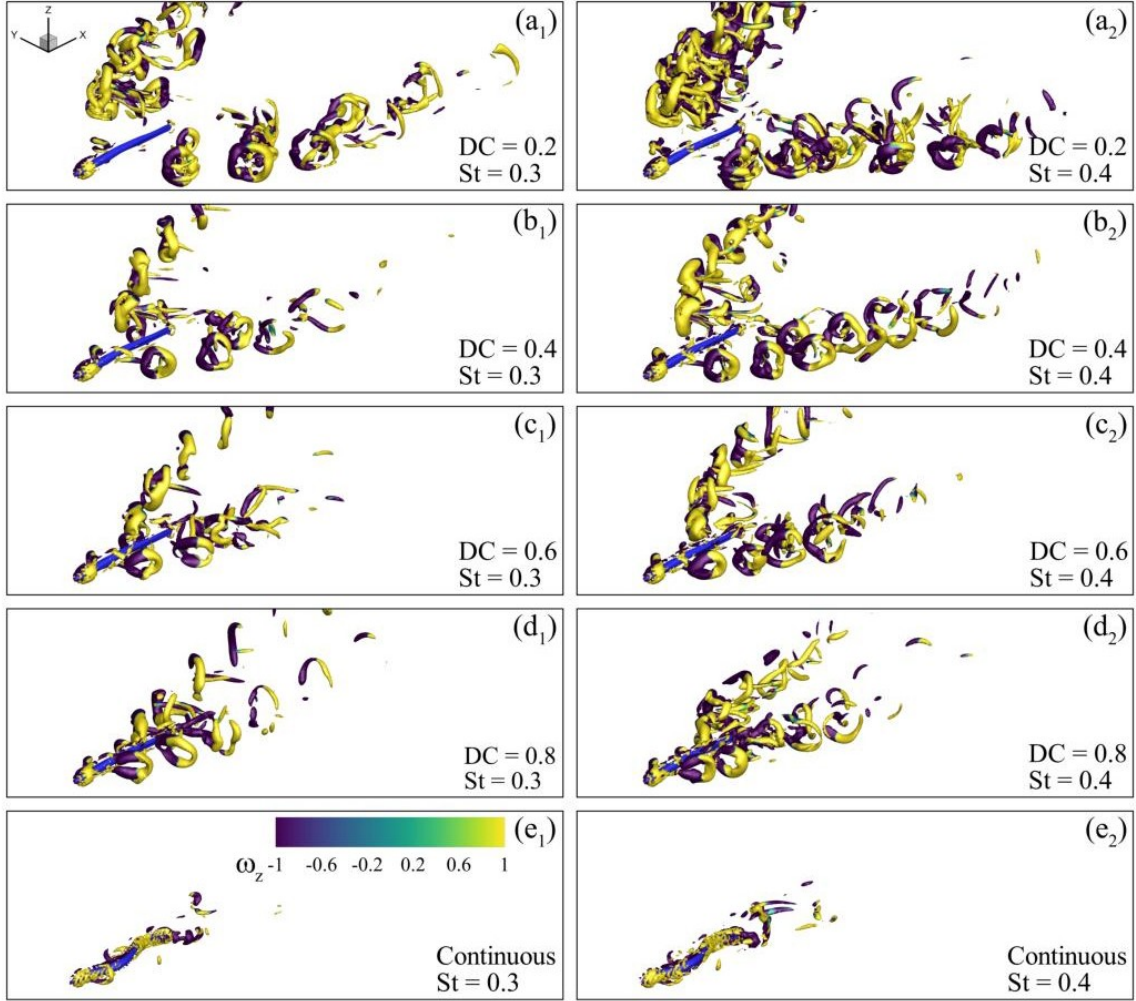


Figure 3: Vortex structures around the anguilliform swimmer at the end of the undulation cycle in 5 modes for (a_1 to e_1) $St = 0.3$ and (a_2 to e_2) $St = 0.4$.

Turning to the carangiform swimmer, visualization in Fig. 4 show the evolution of the wake at the final time instant for all the values of DC and both Strouhal numbers. For $DC = 0.2 - 0.8$, the wake organizes into a bow-like pair of vortex streets that are similar to those of the anguilliform swimmer (Figs. $4a_1$ to $4d_1$ for $St = 0.30$ and Figs. $4a_2$ to $4d_2$ for $St = 0.40$). Two rows detached from the body and lean outward, with the left-sided row persistently steeper in angle. Immediately adjacent to the surface, shear layers roll up into hairpins, which then couple with trailing-edge vortices to be convected downstream. A thin leading-edge shear layer is visible along the anterior part of the body. With an increasing DC, the two rows draw toward the centerline and the number of structures produced per cycle drops, while the angular asymmetry remains evident. Concurrently, the vortices get dissipated in the wake more quickly, as clearly presented in Figs. $4a_1$ to $4d_1$ as an example). Relative to wakes of the anguilliform swimmer in Fig. 3, the flow features around the carangiform swimmer in Fig. 4 show a busier near-body roll-up, producing denser rows and larger, longer-lived vortex structures.

The first important question arise here about the decreasing angle of the bow-shaped wakes for the two swimmers with an increasing values of DC. To understand this behavior, we show the out-of-plane component of vorticity ω_z in the mid plane ($z = 0$) of the flow field in Fig. 5 and label the right- and left-sided vortices along with the bow angles θ_R , θ_L at $DC = 0.4$ and $St = 0.3$. These plots explains the

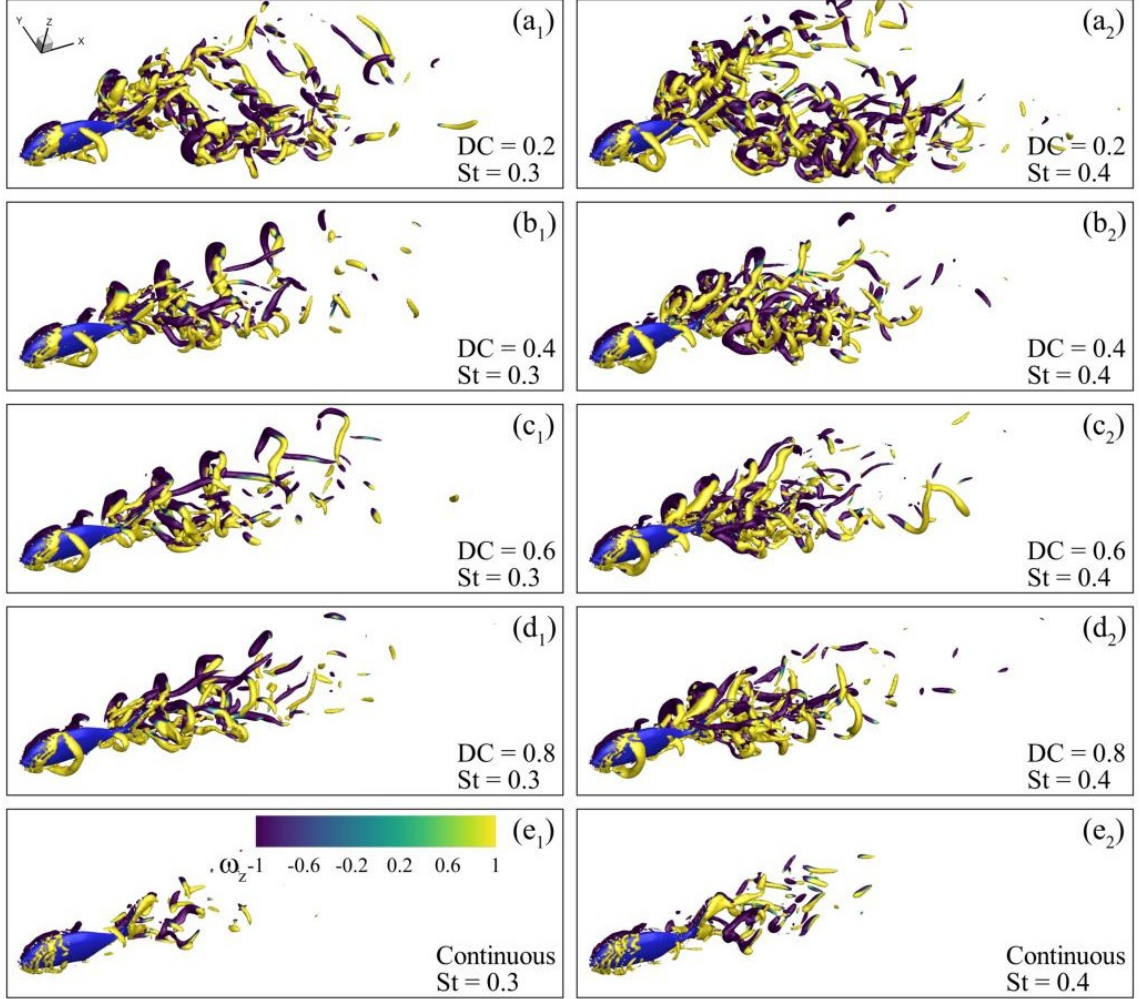


Figure 4: Vortex structures around the carangiform swimmer at the end of the undulation cycle in 5 modes for $(a_1 \text{ to } e_1)$ $St = 0.3$ and $(a_2 \text{ to } e_2)$ $St = 0.4$.

relevant notations and links the two vortex rows to the swimmers' straight bodies. We then track the vortices for the eel and present their streamwise speed (u_x), cross-stream speed (u_y), total speed $|u|$, and the bow angles θ_R and θ_L in Fig. 6 as DC increases from 0.2 to 0.8. These velocities for the vortices V_R and V_L are determined through tracking their centers using the algorithm presented by Khalid et al. [22] and computing the time-averaged values. The plots in Figs. 6a1 and 6a2 demonstrate that both vortices mostly slow down in the streamwise direction, as DC rises, whereas their cross-stream velocity components moves toward zero on each side (see Figs. 6b1 and 6b2). The total speed also drops for $DC > 0.40$ in Figs. 6c1 and 6c2. Most importantly, Figs. 6d1 and 6d2 clearly exhibit that θ_R and θ_L fall toward 0° , and the vortex rows gets deflected inward. This collapse in θ explains how the bow angle decreases with DC. The salient difference in these metrics for the Jack Fish in comparison to those for the eel include: (i) the overall trends for u_x , u_y , $|u|$, θ_R , and θ_L are similar to those of the eel but their change with respect to DC is relatively smaller; (ii) the cross-stream speeds of the two vortices approach each other with less steepness with the increasing DC in the case of the Jack Fish, (iii) the carangiform swimmer's motion is of a large amplitude at the tail and the anterior part of the body performs significantly small-amplitude undulation. Due to this reason, the caudal fin sheds the vortices more axially right from the beginning of the undulation cycle, so a narrower wake is formed. It may leave less room for further narrowing of the wake as we increase DC. Moreover, caudal fin of the Jack Fish holds the leading-edge vortex on its surface for a longer time and guides pairing between the vortices near the trailing edge [10]. It helps stabilize the near-wake and reduces its sensitivity to duty cycle. These important features make the Jack Fish respond less to DC than the eel, which has a slender axisymmetric-like body performing undulations with large amplitudes all along its body.

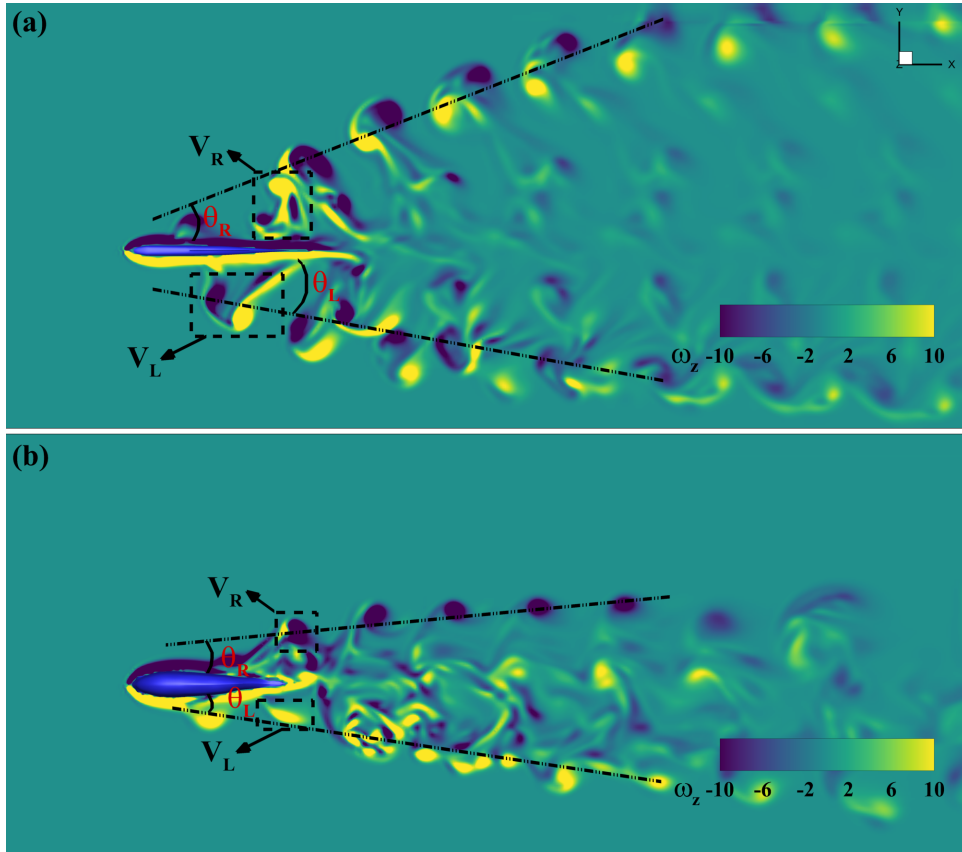


Figure 5: Vorticity (ω_z) at $z = 0$ plane for $DC = 0.4$ at $St = 0.3$ (a) anguilliform swimmer, (b) carangiform swimmer.

In Figs. 6a₁ to d₁, we also see a clear step in u_y when we move from a low to higher DC. For a low DC, the short burst kicks new vortex off the body before other previously shed vortices can pair, so the vortices leave with larger cross-stream speed and form a wide bow. When we extend the time

for the burst phase at a higher DC, the vortices do not get detached from the body at an early stage and traverse along it to do so at a more posterior position. This delay in the detachment of vortices from the swimmer's body help the vortices on the left and right sides of the body become more symmetric. A metric to examine the influence of the formation of the asymmetric vortices on the two sides of the swimmer could be the side force (C_y). Figure 8 provides the plots of the time-averaged C_y for different values of DC and St for both swimmers.

Now, we explain the hydrodynamic forces experienced by the swimmers under different kinematic conditions. Figure 7 shows the mean drag coefficient (\bar{C}_D), averaged over the last five cycles for the eel (anguilliform) and the Jack Fish (carangiform). In Fig. 7a (eel), drag steadily drops as the duty cycle goes from 0.2 to 1.0 for both St = 0.3 and 0.4. These results from the present study corroborate with the findings of Yang et al. [9], where they reported increase in an undulating swimmer's speed through their two-dimensional flow simulations. At a low DC, the higher Strouhal number makes the bursts stronger and more abrupt, so the flow around the body is more disturbed and the average drag is higher. As DC increases, the coast phase gives the flow time to settle, the wake points straighter downstream, and drag keeps reducing for both swimmers (see Fig. 7). Quite interestingly, \bar{C}_D is greater for St = 0.40 than that at St = 0.30 for the intermittent swimming (for all DC < 1.0). Generally, a continuously undulating swimmer's hydrodynamic performance improves in terms of reducing drag, or equivalently increasing thrust, with increasing St [11, 12], as also evident for DC = 1 for the two swimmers in Figs. 7. However, this trend for the influence of St on both swimmers' performance is reversed for the intermittent swimming modes (DC < 1).

Figure 8 shows the time-averaged side force coefficient (\bar{C}_y) for both eel and Jack Fish. For the eel (Fig. 8a), it stays close to zero for all DC and both Strouhal numbers, with a gentle bump around DC = 0.8. This small bump suggests a bit of leftover asymmetry from the mid-body motion at a high DC, but it is mild and goes away again at DC = 1. The side force coefficient of Jack Fish (Fig. 8b) varies more. At low values of DC, the side force is large, especially at St = 0.4. The potential reason could be the stronger bursts pushing the wake sideways, and the jet does not point straight back. When we increase DC, the timing of the vortices traversing to the posterior part of the swimmer and motion of the caudal fin help keep the wake straight and the side force drops fast. It reaches a clear minimum around DC = 0.7~0.8 and then climbs back toward zero when we reach continuous motion.

Figure 9 shows the instantaneous drag coefficient (C_D) for different values of duty cycles at both Strouhal numbers for the eel and Jack Fish. We consider positive C_D as drag and negative C_D as thrust. For the anguilliform swimmer (Fig. 9a₁ and 9a₂) at DC = 1 (continuous), C_D stays close to zero over the whole cycle, and only small oscillations are present. Importantly, this condition indicates the free propulsion of the swimmer, where thrust and drag are balanced, and the swimmer performs steady swimming. In burst and coast motion, the response becomes strongly transient. Right after the burst starts, we see a short-thrust dip (negative C_D) as the body accelerates the fluid, followed by a large drag peak while the body slows down. As DC increases from 0.2 to 0.8, both the thrust dip and the drag peak shrink, and the curve moves back toward the flat continuous baseline. This trend persists at both St = 0.30 and 0.40. Overall, DC appears to be a strong controlling factor to determine how impulsive the temporal profile of the streamwise force looks. On the other hand, the Jack Fish exhibits slightly larger oscillations than the eel but with no large excursions for DC = 1 (see Figs. 9b₁ and 9b₂). For the intermittent kinematics, the burst phase is dominated by drag with short thrust-producing periods. At a low DC, the waveform of the streamwise force often shows three drag peaks and two thrust dips when the swimmer performs bursting motion. These observations might be caused from the initial acceleration and a brief rebound as the tail finishes the burst. As DC increases, all peaks drop in magnitude get further delayed in the kinematic cycle. The effect is strongest at St = 0.4, where the initial burst is more pronounced and produces the largest peaks at low values of DC.

Figure 10 plots the instantaneous side-force coefficient (C_y) for different duty cycles and Strouhal numbers for both swimmers. Positive and negative values indicate force to the right and left, respectively. For the anguilliform swimmer (eel) in Fig. 10a₁ and 10a₂, C_y for the continuous case (DC = 1)

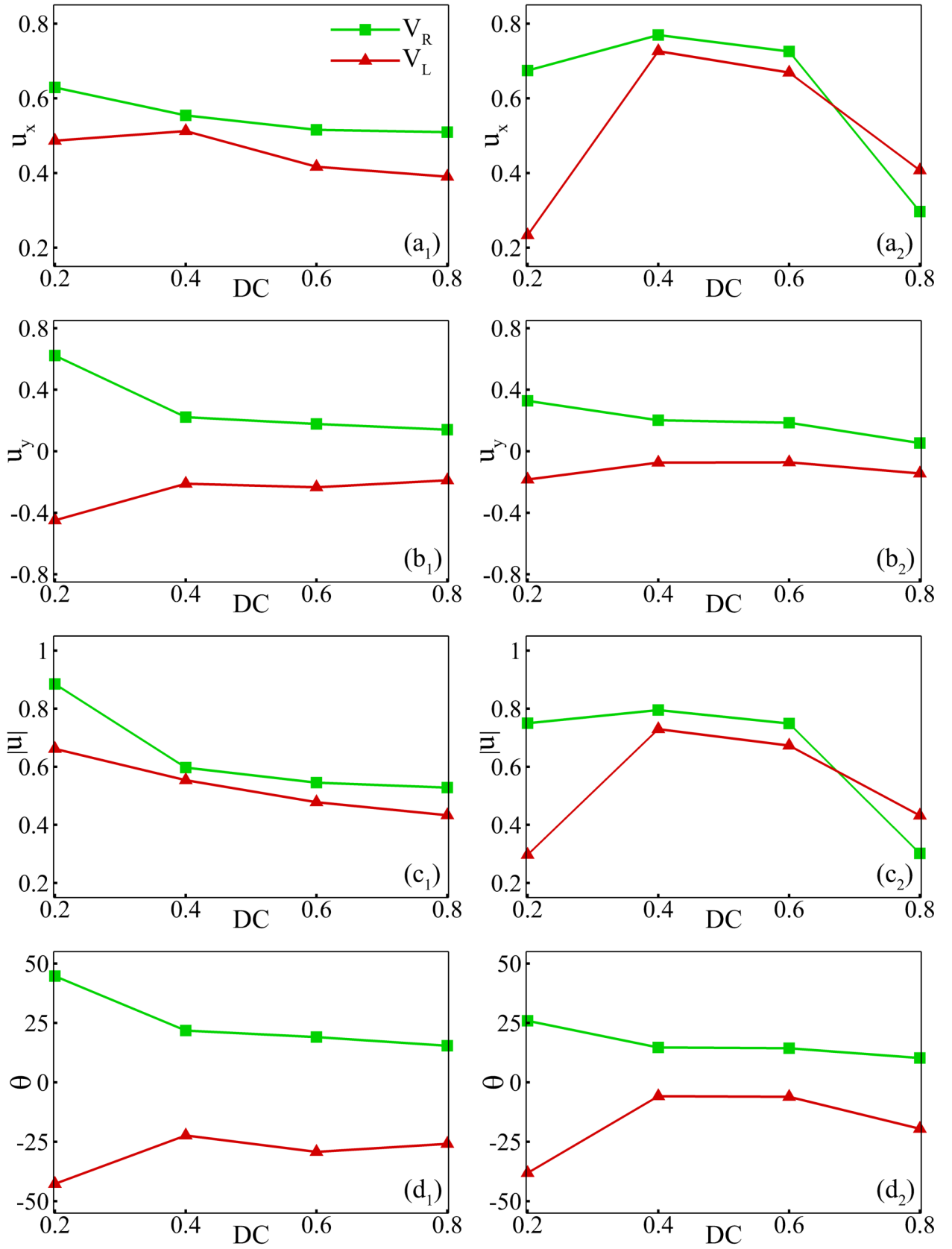


Figure 6: Cycle-averaged kinematic parameters of vortices on the right and left side of a swimmer's body versus DC at St = 0.3 for eel (left column) and Jack Fish (right column), where (a) u_x , (b) u_y , (c) $|u|$, (d) θ_R , and θ_L .

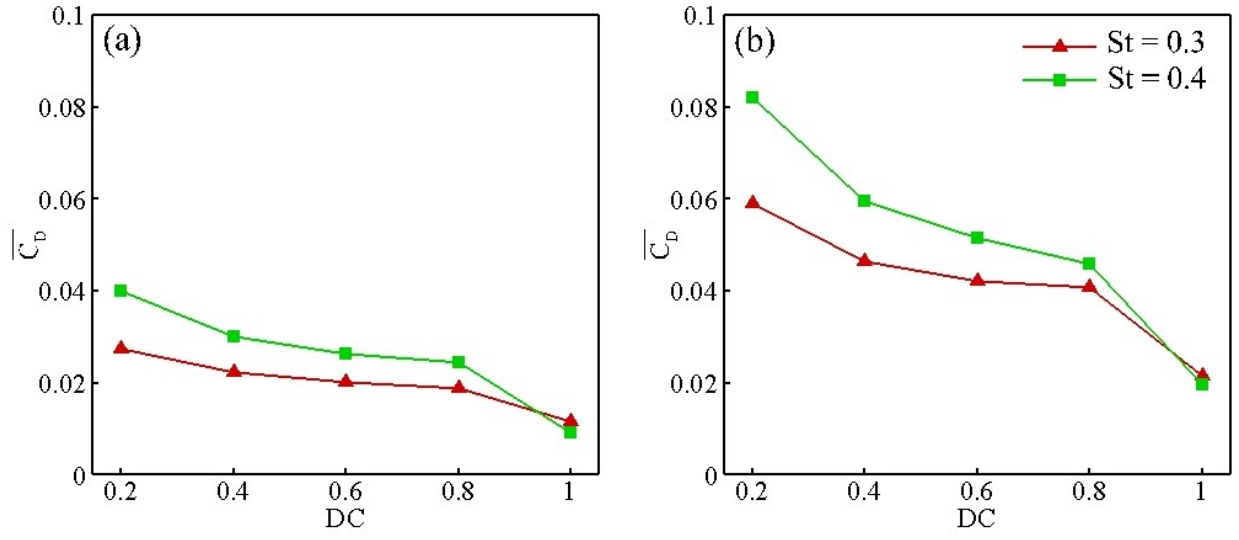


Figure 7: Time-averaged drag coefficient for (a) anguilliform swimmer and (b) carangiform swimmer.

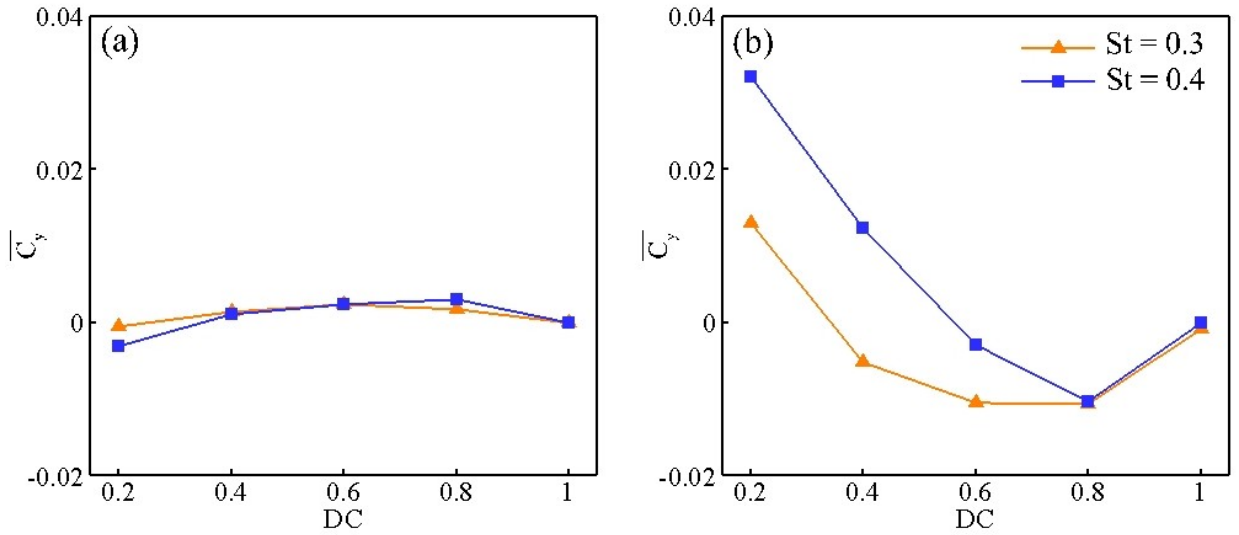


Figure 8: Time-averaged side force coefficient for the (a) anguilliform swimmer and (b) carangiform swimmer.

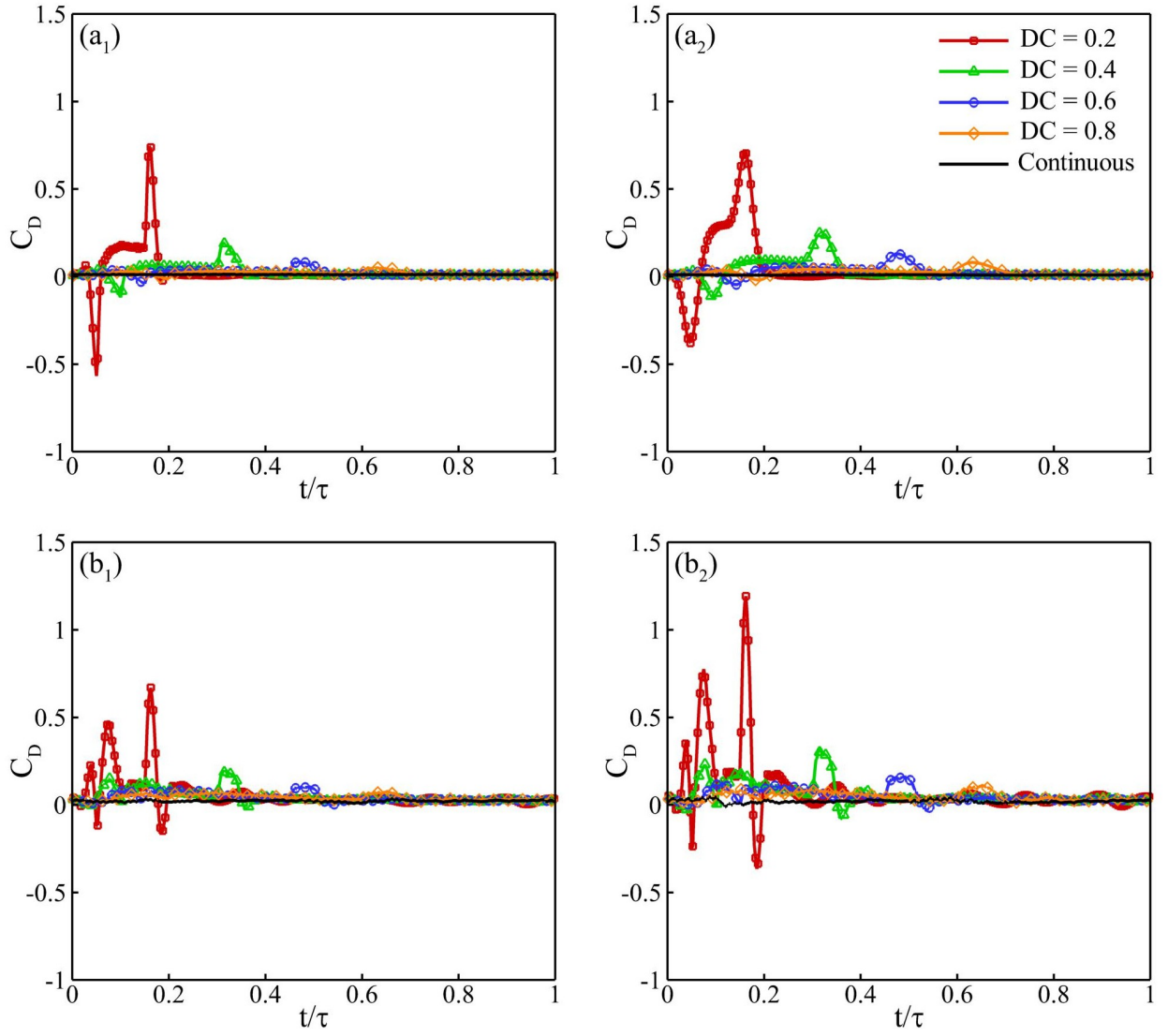


Figure 9: Instantaneous drag force over one cycle in the anguilliform swimmer at (a₁) $St = 0.3$ and (a₂) $St = 0.4$, and in the canrangiform swimmer at (b₁) $St = 0.3$ and (b₂) $St = 0.4$.

is almost flat, showing only slight oscillations. For burst and coast motion of both swimmers, short-lived pulses in C_y appear during the burst window and then fade to near-zero in the coast phase. The pulses are fairly symmetric, a push in one direction is followed by a similar push in the other. As St increases from 0.30 to 0.40, those pulses in the burst phase become more significant. Comparatively, the instant increments and decrements in C_y are larger for the Jack Fish in Figs. 10b₁ and 10b₂. At a low DC, the burst motion often shows a cluster of sharp peaks, which are likely to be linked to the greater tail's acceleration, and a short rebound at the end of the burst. When the coast starts, the side force drops toward zero.

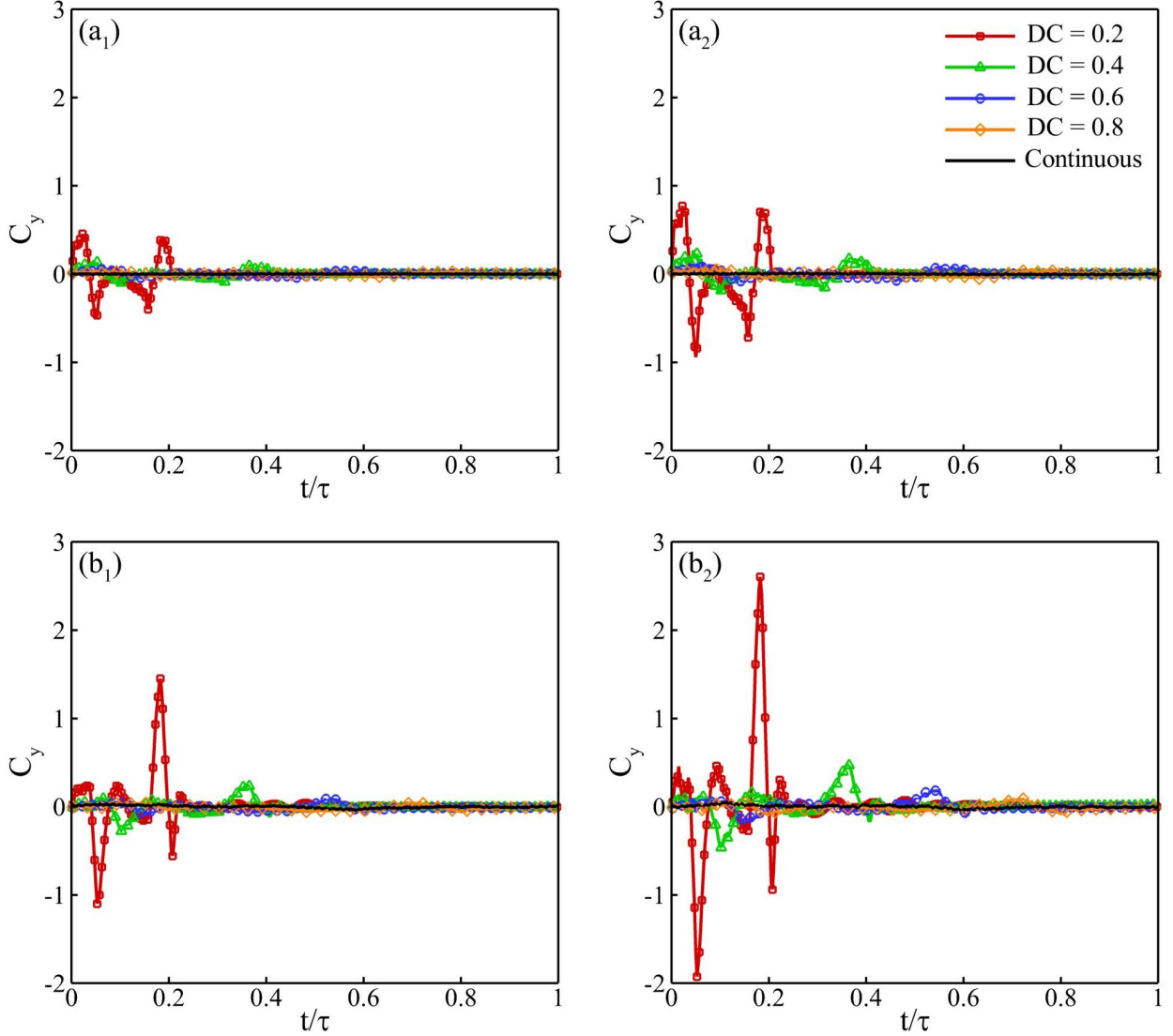


Figure 10: Instantaneous side force over one cycle for the anguilliform swimmer at (a₁) $St = 0.3$ and (a₂) $St = 0.4$, and for the carangiform swimmer at (b₁) $St = 0.3$ and (b₂) $St = 0.4$.

From our previously explained observations, an important question arise about why drag is higher at the greater Strouhal number for the intermittent motion of both the swimmers. To understand the physical mechanisms associated with this aspect, we now analyze the streamwise forces acting on different part of the swimmers' bodies during their different kinematic maneuvers. For this purpose, we project the surface pressure onto the streamwise direction, and plot the local horizontal force as short arrows on the body, considering the mid-plane section of the body in Figs. 11 and 12. It is important to mention that we disregard the influence of shear forces in these computations, following the approach of Gemmel et al. [23] and Du et al. [23]. Here, the blue arrows point downstream and mark drag, whereas the red arrows point upstream and mark thrust. We show three instants within

one cycle to analyze how the pressure-related forces are exerted on different parts of the body. For the anguilliform swimmer, Fig. 11 presents the force profiles for $DC = 0.2$ and 0.6 , as well as continuous undulation at $St = 0.30$. At $DC = 0.2$, the burst starts with strong upstream motion near the tail and lower pressure on the anterior side with the tail and the posterior body generating most of the thrust (see Fig. 11a). Immediately after it happens, we observe a large blue arrows near the tail as the tail slows and the local acceleration reverses. This band marks the impulsive drag that raises the drag in burst and coast motion in Fig. 9a₁. As we raise DC to 0.6 , the band of red arrows at the tail remains there but the blue drag band weakens and shortens in time, as shown in the middle row of plots in Fig. 11. The flow around the mid-body also settles and the patches holding blue arrows shrink. At $DC = 1$ the overall pattern of blue and red arrows seem balanced with the tail still producing more thrust during the kinematic cycle. Nevertheless, the amplitudes of the streamwise pressure-related forces stay small, and we do not see the indications for large impulsive drag events, previously seen for low DC .

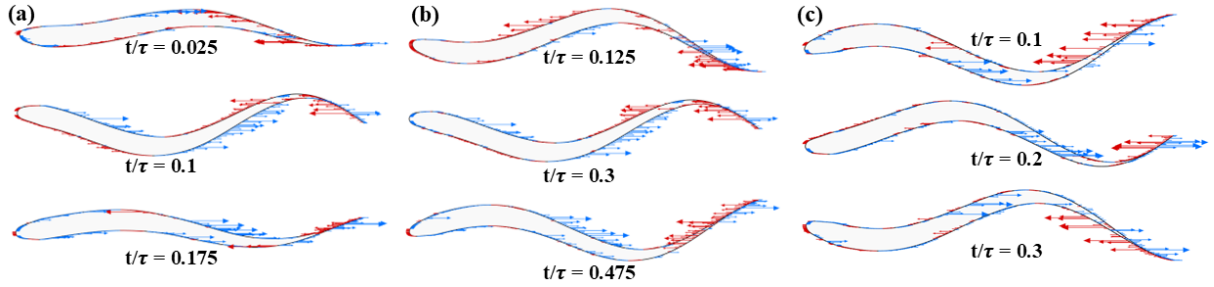


Figure 11: Horizontal forces applied on the anguilliform swimmer body at different time steps at $St = 0.3$ (a) $DC = 0.2$, (b) $DC = 0.6$ and (c) $DC = 1$ (continuous).

For the carangiform swimmer, plots in Fig. 12 show the instantaneous pressure-related forces on the swimmer's body for $DC = 0.2, 0.6$, and 1.0 at $St = 0.3$. At $DC = 0.2$, the tail produces a strong red thrust-indicating band at the start of burst, then a wide blue band over the caudal fin during the stroke reversal. That blue-arrow band marks the main drag source in burst and coast for the Jack Fish. As we increase DC to 0.6 , the cluster of blue arrows weakens and gets shortened, and the mid-body carries a larger share of nearly symmetric loads. In the case for continuous motion, the region near the peduncle and the tail experience larger streamwise forces. Here, the flow looks more streamlined, traversing along the body, in comparison to the eel, because the tail is able to produce a more axially-oriented wake from the beginning of the motion. These physical mechanisms explain the smaller side-force and drag slopes for the Jack Fish with an increasing DC in Figs. 9b₁ and 10b₁.

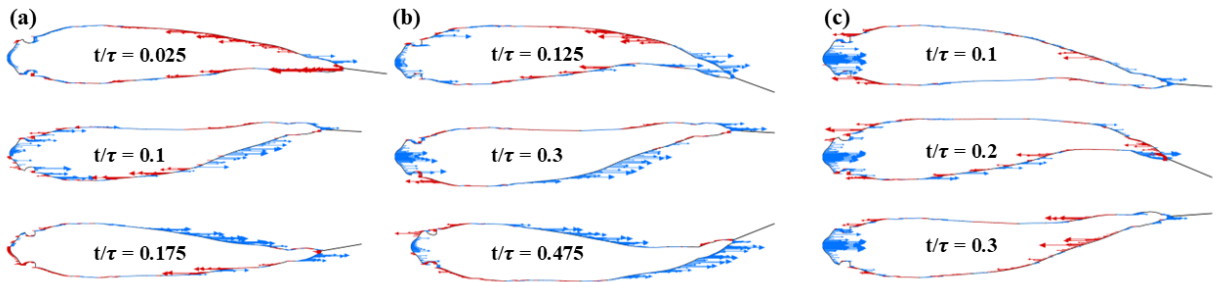


Figure 12: Horizontal forces experienced by the carangiform swimmer body at different time instants for $DC =$ (a) 0.20 , (b) 0.6 and (c) 1.0 at $St = 0.30$.

Although the overall streamwise force coefficient C_D is already quantified and presented previously, it is insightful to focus solely on quantifying the pressure-component of the forces indicated in Figs. 12 and 12. Therefore, we plot the cycle-averaged drag and thrust caused by pressure along the whole body, and their net metric for each DC and St in for both swimmers in Fig. 13. In the case of the anguilliform swimmer (see Figs. 13a₁, 13b₁, and 13c₁), there are a few clear observations. Looking

at the drag profiles (Fig.13 a_1 for eel and Fig. 13 a_2 for Jack Fish), it is evident that the cases with higher St produces substantially more drag for all $DC < 1$. For the case of $DC = 1$, the eel produces slightly greater drag at $St = 0.40$ compared to that on $St = 0.3$ from the pressure component of the streamwise force. However, the Jack Fish produces significantly less drag at the greater value of St . In the thrust profiles (see Figs. 13 b_1 and 13 b_2), we see similar observations for the two swimmers. The only difference is that the Jack Fish produces comparatively larger thrust for $St = 0.40$ and $DC = 1.0$. The total (net) force in Figs. 13 c_1 and 13 c_2 . shows how the overall drag is more for the higher Strouhal number for all $DC < 1$ for both anguilliform and carangiform swimmers. These observations also relate very well the profiles of \bar{C}_D presented in Fig. 7.

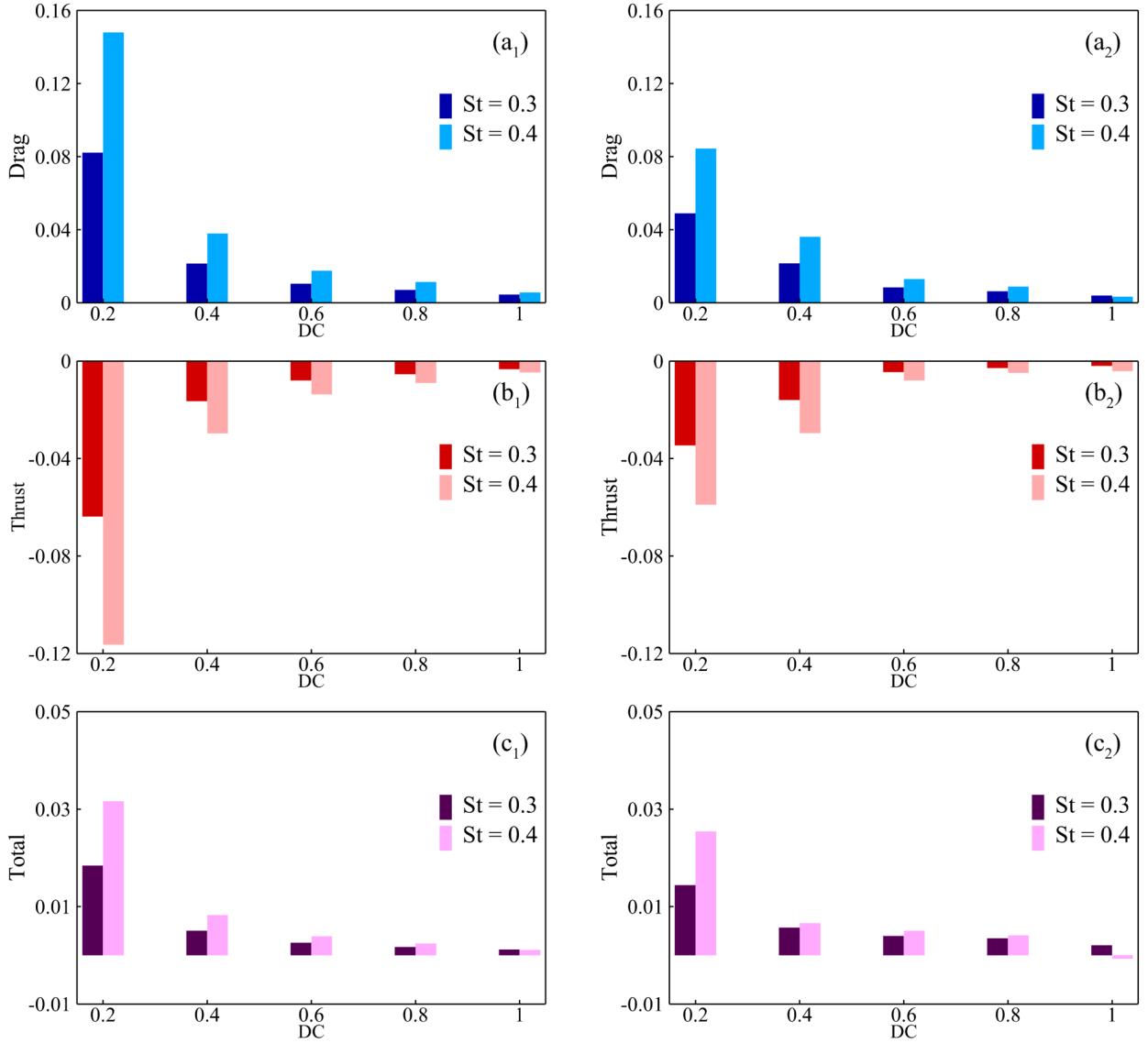


Figure 13: Cycle-averaged pressure forces versus duty cycle DC for anguilliform (a_1, b_1, c_1) and carangiform (a_2, b_2, c_2) swimmers: drag (top), thrust (middle), and net (bottom) at $St = 0.3$ and $St = 0.4$.

The next important aspect of the instantaneous hydrodynamic streamwise force in Fig. 9 relates to larger peaks for low values of DC compared to its larger values. In order to elucidate this phenomenon, it is logical to quantify the strength of the vortices shed from the body under different kinematic conditions, as this metric directly relates to the magnitude of the hydrodynamic forces, experienced by the swimmer. Hence, we track circulation (Γ) of the right and left vortices marked earlier in Fig. 5 and compare three cases for each gait: $DC = 0.2$, $DC = 0.6$, and continuous undulation at $St = 0.3$ in Fig. 14. Please note that Figs. 14 a_1 14 b_1 provides the plots for instantaneous circulation of the vortices initially shed from the right and left sides, respectively, of the eel, whereas Figs. 14 a_2 14 b_2 provide Γ

for their counterparts around the Jack Fish. It is also important to mention that the purpose of these plots are to quantify the strength of the first vortices shed from the two sides of the swimmers, regardless of their orientation. All these plots make it evident from the magnitudes of Γ that the vortices formed and shed on the two sides of both the swimmers are stronger for small DC. They also keep their comparative strength intact while traversing in the wake after getting shed from the bodies and interacting with other secondary flow structures in the wakes.

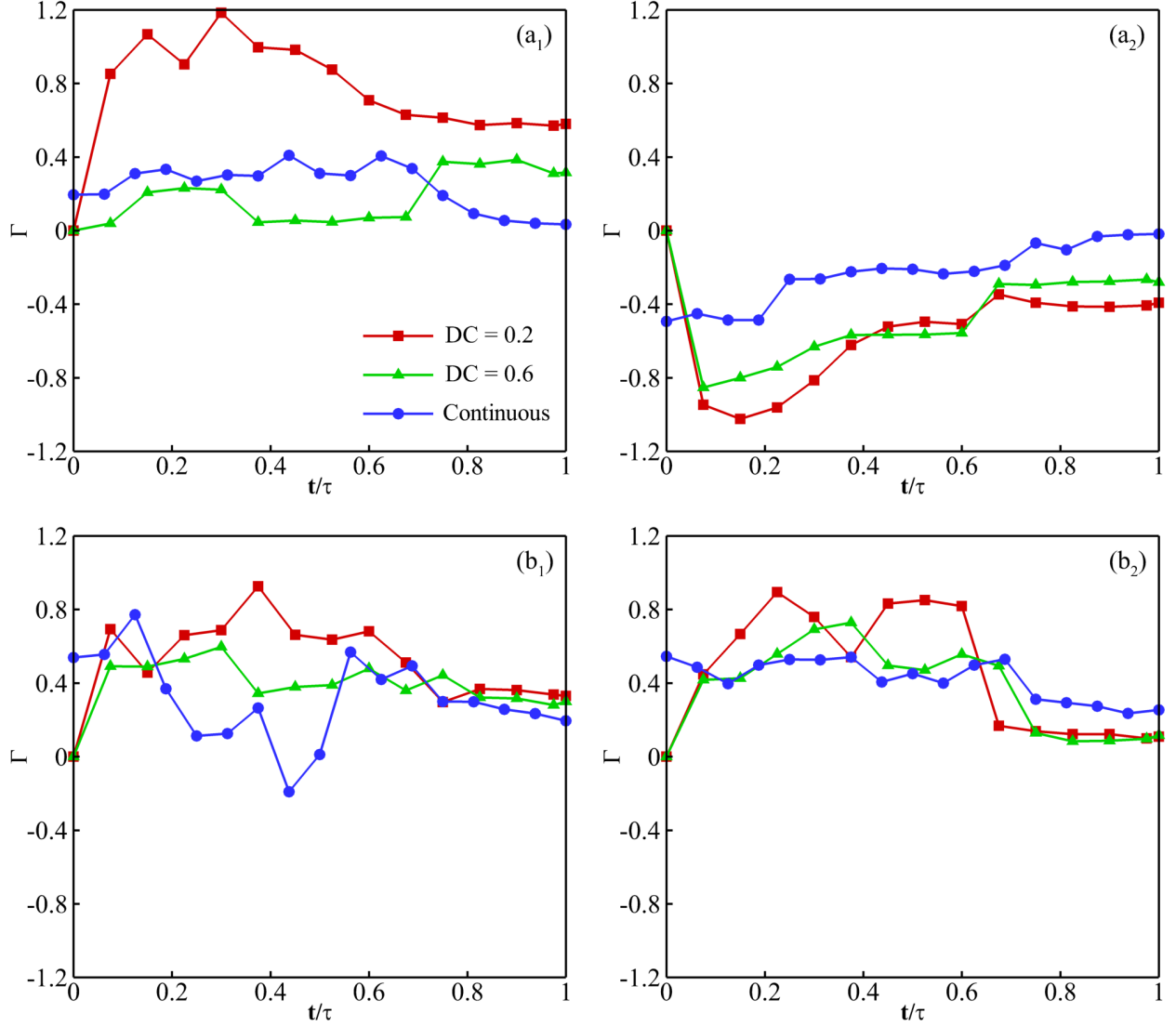


Figure 14: Circulation of the (a₁) right-sided vortex and (b₁) left-sided vortex around the eel, and that of the (a₂) right-sided vortex and (b₂) left-sided vortex around the Jack fish

4 Conclusions

Undulatory marine swimmers attain their hydrodynamic performance by controlling how near-body vortices grow, get shed, and form the wake. In this study, we examine how duty cycle, as an important feature of the burst-and-coast motion of carangiform and anguilliform swimmers, influence vortex dynamics and formation of the wakes and affect the generation of unsteady hydrodynamic forces. This work reveals the formation of a bow-shaped wake for smaller values of DC, which further becomes more streamwise as the two rows of vortices from the left and right sides of the swimmer approach each other with an increasing value of DC. Our results provide evidence for how DC controls the bow angle in such cases. Secondly, we explain the greater drag in burst-and-coast motion for the higher

Strouhal number, that is contrary to what is usually observed for continuously undulating swimmers. Furthermore, the eel forms a largely spread wake with higher bow angles during the intermittent swimming, where the carangiform swimmer demonstrates lesser sensitivity to this feature as a function of DC primarily due to the substantial motion of the posterior parts of the body. We also explain the mean and instantaneous hydrodynamic forces for different values of duty cycle and Strouhal number, that provide new insights about the hydrodynamic behavior of two entirely different kinematics and morphologies of biological swimmers.

Acknowledgment

MSU Khalid acknowledges funding support from the Natural Sciences and Engineering Research Council of Canada (NSERC) through the Discovery and Alliance International grant programs for this work. A. Tarokh also thanks NSERC for their support through the Discovery grant. The simulations reported in this work were performed on the supercomputing clusters administered and managed by the Digital Research Alliance of Canada.

References

- [1] Laura A Miller and Charles S Peskin. When vortices stick: an aerodynamic transition in tiny insect flight. *Journal of Experimental Biology*, 207(17):3073–3088, 2004.
- [2] Iman Borazjani and Fotis Sotiropoulos. Numerical investigation of the hydrodynamics of anguilliform swimming in the transitional and inertial flow regimes. *Journal of Experimental Biology*, 212(4):576–592, 2009.
- [3] Muhammad Saif Ullah Khalid, Junshi Wang, Imran Akhtar, Haibo Dong, Moubin Liu, and Arman Hemmati. Larger wavelengths suit hydrodynamics of carangiform swimmers. *Physical Review Fluids*, 6(7):073101, 2021.
- [4] Michael Sfakiotakis, David M Lane, and J Bruce C Davies. Review of fish swimming modes for aquatic locomotion. *IEEE Journal of oceanic engineering*, 24(2):237–252, 2002.
- [5] Ruosi Liu, Qiye Yang, Yang Ding, and Guangming Xie. Intermittent swimming demonstrates energy-saving capabilities: experimental evidence from robotic fish. *Ocean Engineering*, 340:122335, 2025.
- [6] Theodore Yaotsu Wu. Fish swimming and bird/insect flight. *Annual review of fluid mechanics*, 43(1):25–58, 2011.
- [7] Longzhen Dai, Guowei He, Xiang Zhang, and Xing Zhang. Intermittent locomotion of a fish-like swimmer driven by passive elastic mechanism. *Bioinspiration & biomimetics*, 13(5):056011, 2018.
- [8] Gen Li, Dmitry Kolomenskiy, Hao Liu, Ramiro Godoy-Diana, and Benjamin Thiria. Intermittent versus continuous swimming: An optimization tale. *Physical Review Fluids*, 8(1):013101, 2023.
- [9] Dewu Yang, Jie Wu, Kaustubh Khedkar, Li-Ming Chao, and Amneet Pal Singh Bhalla. Hydrodynamics and scaling laws for intermittent s-start swimming. *Journal of Fluid Mechanics*, 984:A2, 2024.
- [10] Iman Borazjani and Fotis Sotiropoulos. Numerical investigation of the hydrodynamics of carangiform swimming in the transitional and inertial flow regimes. *Journal of experimental biology*, 211(10):1541–1558, 2008.

- [11] Geng Liu, Yan Ren, Haibo Dong, Otar Akanyeti, James C Liao, and George V Lauder. Computational analysis of vortex dynamics and performance enhancement due to body–fin and fin–fin interactions in fish-like locomotion. *Journal of fluid mechanics*, 829:65–88, 2017.
- [12] Muhammad Saif Ullah Khalid, Junshi Wang, Imran Akhtar, Haibo Dong, Moubin Liu, and Arman Hemmati. Why do anguilliform swimmers perform undulation with wavelengths shorter than their bodylengths? *Physics of Fluids*, 33(3), 2021.
- [13] Amirhossein Fardi, Hamayun Farooq, Imran Akhtar, Arman Hemmati, and Muhammad Saif Ullah Khalid. Characterizing the role of hind flippers in hydrodynamics of a harbor seal. *Bioinspiration & Biomimetics*, 20(4):046010, 2025.
- [14] Emre Akoz and Keith W Moored. Unsteady propulsion by an intermittent swimming gait. *Journal of Fluid Mechanics*, 834:149–172, 2018.
- [15] Intesaaf Ashraf, Sam Van Wassenbergh, and Siddhartha Verma. Burst-and-coast swimming is not always energetically beneficial in fish (hemigrammus bleheri). *Bioinspiration & biomimetics*, 16(1):016002, 2020.
- [16] JJ Videler and F Hess. Fast continuous swimming of two pelagic predators, saithe (*pollachius virens*) and mackerel (*scomber scombrus*): a kinematic analysis. *Journal of experimental biology*, 109(1):209–228, 1984.
- [17] Hamayun Farooq, Imran Akhtar, Arman Hemmati, and Muhammad Saif Ullah Khalid. An accurate immersed boundary method using radial-basis functions for incompressible flows. *Journal of Computational Physics*, 531:113928, 2025.
- [18] Rajat Mittal, Haibo Dong, Meliha Bozkurtas, FM Najjar, Abel Vargas, and Alfred Von Loebbecke. A versatile sharp interface immersed boundary method for incompressible flows with complex boundaries. *Journal of computational physics*, 227(10):4825–4852, 2008.
- [19] Maham Kamran, Amirhossein Fardi, Chengyu Li, and Muhammad Saif Ullah Khalid. On the role of morphology and kinematics of biological swimmers to spread and suppress their odors in the wake. *arXiv preprint arXiv:2503.14648*, 2025.
- [20] Qiang Zhong, Haibo Dong, and Daniel B Quinn. How dorsal fin sharpness affects swimming speed and economy. *Journal of Fluid Mechanics*, 878:370–385, 2019.
- [21] Frank E Fish. Advantages of aquatic animals as models for bio-inspired drones over present auv technology. *Bioinspiration & biomimetics*, 15(2):025001, 2020.
- [22] Muhammad Saif Ullah Khalid, Junshi Wang, Haibo Dong, and Moubin Liu. Flow transitions and mapping for undulating swimmers. *Physical Review Fluids*, 5(6):063104, 2020.
- [23] Brad J Gemmell, Stephanie M Fogerson, John H Costello, Jennifer R Morgan, John O Dabiri, and Sean P Colin. How the bending kinematics of swimming lampreys build negative pressure fields for suction thrust. *Journal of Experimental Biology*, 219(24):3884–3895, 2016.